

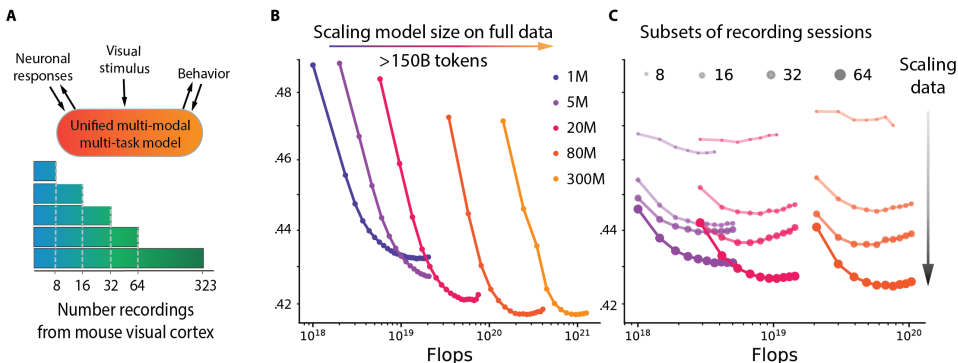
# 000 001 OMNIMOUSE: SCALING PROPERTIES OF MULTI-MODAL, 002 MULTI-TASK BRAIN MODELS ON 150B NEURAL TOKENS 003 004

005 **Anonymous authors**

006 Paper under double-blind review

## 007 008 ABSTRACT 009

011 Scaling data and artificial neural networks has transformed AI, driving break-  
012 throughs in language and vision. Whether similar principles apply to modeling  
013 brain activity remains unclear. Here we leveraged a dataset of 3.3 million neu-  
014 rons from the visual cortex of 78 mice across 323 sessions, totaling more than  
015 150 billion neural tokens recorded during natural movies, images and param-  
016 etric stimuli, and behavior. We train multi-modal, multi-task transformer models  
017 (1M–300M parameters) that support three regimes flexibly at test time: neural  
018 prediction (predicting neuronal responses from sensory input and behavior), be-  
019 havioral decoding (predicting behavior from neural activity), neural forecasting  
020 (predicting future activity from current neural dynamics), or any combination of  
021 the three. We find that performance scales reliably with more data, but gains from  
022 increasing model size saturate – suggesting that current brain models are limited  
023 by data rather than compute. This inverts the standard AI scaling story: in lan-  
024 guage and computer vision, massive datasets make parameter scaling the primary  
025 driver of progress, whereas in brain modeling – even in the mouse visual cortex, a  
026 relatively simple and low-resolution system – models remain data-limited despite  
027 vast recordings. These findings highlight the need for richer stimuli, tasks, and  
028 larger-scale recordings to build brain foundation models. The observation of sys-  
029 tematic scaling raises the possibility of phase transitions in neural modeling, where  
030 larger and richer datasets might unlock qualitatively new capabilities, paralleling  
the emergent properties seen in large language models.



031  
032 Figure 1: **A.** OmniMouse unifies neural prediction, behavior decoding, and forecasting tasks. **B.**  
033 Scaling model size on an 150+ billion neural tokens shows performance saturation, unlike language  
034 models. **C.** In contrast, scaling data consistently improves performance across all model sizes, sug-  
035 gesting that neural prediction is currently limited by data.

## 036 037 038 1 INTRODUCTION 039 040

041 Scaling models and data has driven recent progress in machine learning, with large language, vision,  
042 and multi-modal models showing consistent performance gains and enabling foundation models that  
043 unify tasks across domains. A natural question is whether models of the brain can also benefit from  
044 scaling. In the mouse visual cortex, large datasets (MICrONS Consortium et al., 2021; de Vries  
045

et al., 2019; Angelaki et al., 2025) and standardized benchmarks (Willeke et al., 2022; Turishcheva et al., 2024) exist. Yet, compared with internet-scale corpora, the available datasets are much smaller, more fragmented, and less diverse. The neuroscience community has recently started to work towards foundational models for EEG (Chau et al., 2024; Chen et al., 2024; Cui et al., 2024; Jiang et al., 2024; Kostas et al., 2021; Yang et al., 2023; Thapa et al., 2024; Li et al., 2024), fMRI (Caro et al., 2023; Dong et al., 2024; Kan et al., 2022; Thomas et al., 2022; d’Ascoli et al., 2025), MEG (Csaky et al., 2024), and intracranial signals (Zhang et al., 2023; Wang et al., 2023). But single-neuron resolution, multi-modal foundation models are still missing.

Prior work in this direction focused on isolated modalities (Ye et al., 2023; Azabou et al., 2023), a single predictive task (Wang et al., 2025), lacked scalability across datasets (Ye & Pandarinath, 2021; Mi et al., 2023; Antoniades et al., 2024), or omitted stimulus and behavioral information (Jiang et al., 2025; Mi et al., 2023). These models do not capture the multi-modal and multi-task nature of neural computation. Hence, we cannot systematically study if there are benefits of scaling – a key hallmark of foundational models – in large-scale, single-neuron recordings.

In this work, we introduce OmniMouse, a multi-modal, multi-task architecture for modeling activity in the mouse visual cortex. OmniMouse integrates video stimuli, neuronal responses, and behavioral signals (running speed, eye movements and pupil size) into a single transformer framework. Unlike prior models restricted to a single modality, task or dataset, it supports diverse prediction tasks, including neural forecasting (predicting from past activity), video-to-response prediction, and decoding behavior from neuronal activity. We train OmniMouse on the largest single-neuron dataset: 323 recordings from the visual cortex of 78 awake mice, with over 150 billion neuronal activity tokens. Mice were shown naturalistic movies, images, and parametric stimuli. The unprecedented scale of this dataset allows us to study how model and dataset size shape predictive performance and if the scaling improvements seen in language and vision extend to large-scale single-neuron recordings.

Our main findings and contributions are:

- **We propose a versatile multi-modal multi-task model:** OmniMouse handles both single-modality and multi-modal, supporting any combination of forecasting and stimulus-conditioned prediction across neurons, stimuli, time, and animals in a single model.
- **We demonstrate the benefits of scaling:** Larger models and datasets improve predictions, with OmniMouse surpassing specialized state-of-the-art models across all tasks.
- We find that performance plateaus beyond moderate model sizes, which suggests that predictive accuracy may currently be constrained by data rather than model size or compute.

## 2 RELATED WORK

**Large-scale deep learning models for single-neuron predictions.** Deep learning has advanced predictive modeling in neuroscience, particularly in vision (Cadieu et al., 2014; Batty et al., 2017; Klindt et al., 2017; McIntosh et al., 2016; Cadena et al., 2019; Kindel et al., 2019; Walker et al., 2019; Zhang et al., 2018; Ecker et al., 2018; Sinz et al., 2018; Burg et al., 2021; Cowley & Pillow, 2020). Early CNN-based approaches introduced shared feature cores with per-neuron readouts (Antolík et al., 2016; Klindt et al., 2017; McIntosh et al., 2016), later extended with temporal dynamics (Sinz et al., 2018) and more efficient readouts (Lurz et al., 2021). Building on these advances, Wang et al. (2025) trained a 13-mice CNN model and showed that “digital twins” can capture biological phenomena beyond their training data. With the shift to transformers, new variants have explored ViT cores (Li et al., 2023), hybrid convolution-attention designs (Lin et al., 2024; Pierzchlewicz et al., 2023), and spatial-transformer readouts (Saha et al., 2024), though most still omit video input.

Transformers have also been applied to response-to-response modeling. The Neural Data Transformer (NDT) (Ye & Pandarinath, 2021) predicted spikes from spikes and behavior, later extended to multiple animals (Ye et al., 2023) and neuronal masking strategies (Zhang et al., 2024). While NDT projects all neurons together via linear layers, Quantformer (Calcagno et al., 2024), also a transformer-based forecaster, introduced neuron-specific tokens to handle any number of neurons. POYO (Azabou et al., 2023), a behavior-decoding model, added spike timing to similar tokens, removing the need for time-window binning, and its extension POYO+ (Azabou et al., 2025) also handled discrete classification tasks such as stimulus orientation. POCO (Duan et al., 2025) combined POYO and NDT tokenization to predict neuronal activity from history and other neurons, while

108 STDNT (Le & Shlizerman, 2022) explicitly modeled correlations but did not consistently outperform  
 109 NDT. The aforementioned models ignore visual stimuli. To study the combined effect of both the  
 110 ‘brain state’ and ‘visual stimuli’ on neuronal activity, Bashiri et al. (2021) used a CNN branch for pro-  
 111 cessing static input stimuli and an additional flow-branch to model trial-to-trial correlations between  
 112 neurons. For dynamic video stimuli, Schmidt et al. (2025) modeled a latent brain state probabilisti-  
 113 cally, using NDT-style response tokenization. Similarly, Neuroformer (Antoniades et al., 2024) used  
 114 past activity and visual input but is limited to single sessions and cannot flexibly condition on subsets  
 115 of neurons or response history. CEBRA (Schneider et al., 2023), a contrastive encoder, also mapped  
 116 activity to behavior or stimuli, accounting for inter-neuron correlations.

117 The closest work to ours, outside of single-cell studies, is d’Ascoli et al. (2025). They built a multi-  
 118 modal fMRI predictor using concatenated video, text, and audio embeddings from pretrained back-  
 119 bones and used modality dropout and a subject-specific loss, but did not use other voxels as input.

120 **General scaling laws in deep learning.** Large-scale models in language and vision exhibit pre-  
 121 dictable improvements with scale, described by empirical “scaling laws”. Kaplan et al. (2020) first  
 122 showed that performance follows power-law trends in model size, dataset size, and compute. Hoff-  
 123 mann et al. (2022) refined this with “Chinchilla scaling”, prescribing proportional growth of model  
 124 and data size for optimal efficiency. Aghajanyan et al. (2023) adjusted scaling laws for models  
 125 with large per-modality pre-trained tokenizers but newer lightweight tokenization (“early-fusion”)  
 126 approaches (Chameleon, 2024; Piergiovanni et al., 2024; Shukor et al., 2025) achieved stronger per-  
 127 formance with fewer parameters. Hence, no universal framework for multi-modal scaling exists:  
 128 Shukor et al. (2025) estimated power-law coefficients for early-fusion models but did not analyze  
 129 cross-modal interactions. This gap is especially evident in scientific domains, where data are multi-  
 130 modal, complex, noisy, and limited. Examples such as AlphaFold3 (Abramson et al., 2024) suggest  
 131 that systematic scaling of both models and datasets can drive major advances in AI for science.

132 **Scaling neuroscience models.** There is no consensus on whether classic machine learning scal-  
 133 ing laws apply to single-neuron data. Jiang et al. (2025) questioned their applicability, analyzing  
 134 the NDT-based model of Zhang et al. (2025), which predicted ~30,000 spiking neurons across 74  
 135 sessions. Jiang et al. (2025) argued that cross-session variability – and thus implicit data heterogene-  
 136 ity – is crucial for scaling benefits, though it remains unclear if these results generalize to different  
 137 mouse tasks or model architectures. Again using an NDT-based model but on EEG data, Ye et al.  
 138 (2025) reported that scaling is constrained by data variability, which pretraining alone cannot fully  
 139 overcome. Consistent with this view, POCO (Duan et al., 2025) used calcium imaging to show that  
 140 longer recordings improve predictive performance, aligning with earlier results of Lurz et al. (2021).  
 141 However, POCO included fewer than 90,000 neurons, mostly from zebrafish (~77,000). Neural sat-  
 142 uration has also been observed: Gokce & Schrimpf (2024) found that behavioral alignment improves  
 143 with model size, but neural alignment plateaus, with gains concentrated in higher-level visual ar-  
 144 eas. In contrast, Antonello et al. (2023) reported no such saturation when predicting language and  
 145 audio fMRI responses, suggesting that scaling limits may depend on the modality and data regime.  
 146 The largest single-cell response-to-behavior prediction model is POYO+ Azabou et al. (2025) with  
 147 ~100,000 neurons, which did not analyze scaling. Together, these findings highlight the need for  
 148 large, multi-modal, single-neuron datasets to test how scaling laws manifest in systems neurosciences.

### 3 LARGE-SCALE SINGLE-NEURON DATASET

152 Data were collected from head-fixed mice running on a wheel while viewing visual stimuli consist-  
 153 ing of both images and movies (Fig. 2). Neuronal activity was recorded alongside several behav-  
 154 ioral variables: locomotion speed, pupil center positions ( $x$  and  $y$ ), pupil diameter, and its temporal  
 155 derivative. These behavioral signals are widely used as proxies for modulatory effects on neuronal  
 156 responses (Niell & Stryker, 2010; Reimer et al., 2014).

157 **Neuronal responses.** We used a dataset of over 3 million single-unit neuronal recordings – an or-  
 158 der of magnitude larger than the recently published Brain-Wide Map dataset (BWD, 621,733 neu-  
 159 rons) (Angelaki et al., 2025). The dataset contains excitatory neurons’ responses in visual cortex  
 160 recorded via wide-field two-photon calcium imaging at 6–14 Hz in awake, head-fixed, behaving mice  
 161 (Sofroniew et al., 2016), with spiking activity extracted by CAIMAN (Giovannucci et al., 2019), up-  
 sampled linearly to 30 Hz for all recordings.

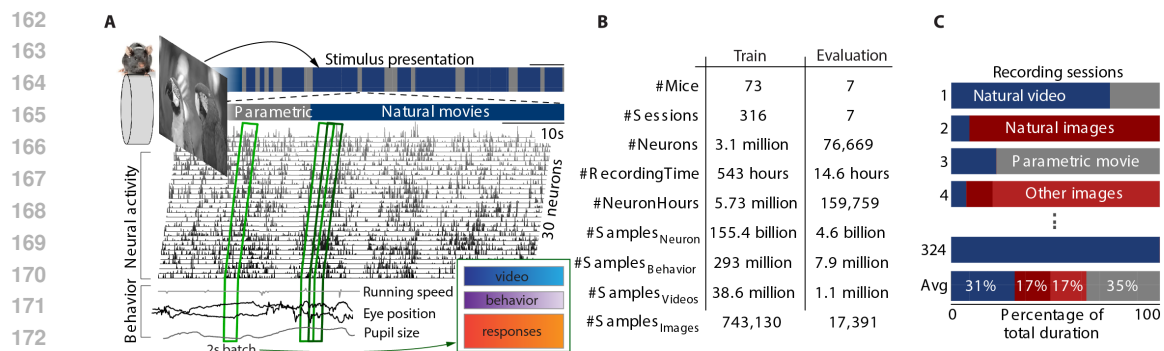


Figure 2: **Data.** A. Data were collected from head-fixed mice running on a wheel while viewing videos. Neuronal responses were recorded via calcium imaging, 4210 to 11284 neurons per session. Behavior variables include pupil center  $x$  and  $y$  positions, pupil dilation and its derivative and running speed. B. Dataset statistics. The total number of unique mice in our dataset is 78, since some mice had sessions in both train and evaluation sets. C. Different visual stimuli were presented across sessions, with stimulus types varying by session. The bottom row shows their overall distribution.

**Visual stimuli.** The mice were presented with naturalistic images sampled from ImageNet (Russakovsky et al., 2015) and videos sampled from cinematic movies and the Sports-1M dataset (Karpathy et al., 2014). In addition, they saw parametric stimuli such as static and drifting Gabor (Petkov & Subramanian, 2007), directional pink noise, flashing Gaussian dots, random dot kinematograms (Morrone et al., 2000), and model-generated stimuli (similar to Walker et al., 2019). All stimuli were shown at 30–60 Hz, with images presented for 500 ms and preceded by a 300–500 ms blank screen.

**Data utilization.** A key novelty is our ability to sample arbitrary 2-second windows from any point in the experiment, including inter-trial intervals and blank screens. We reconstruct the visual stimulus presented with millisecond precision throughout the entire recording, enabling continuous representation of the full experimental timeline. This dramatically increases training data by utilizing the complete recording duration rather than discrete trials.

## 4 OMNIMOUSE ARCHITECTURE

**Tokenization.** We sample 2-second chunks of multi-modal data: video frames  $\mathbf{V} \in \mathbb{R}^{h \times w \times 1 \times 60}$ , neural calcium traces  $\mathbf{X} \in \mathbb{R}^{P \times 60}$  for population  $P$ , and behavioral traces  $\mathbf{B} \in \mathbb{R}^{5 \times 40}$  (running speed, pupil  $xy$ -position / size / size derivative). Alongside the chunk, we sample a masking configuration for each modality.

For *video*, the sampled mask defines a starting frame  $v_0$  and the length of visible frames  $v_c$  such that  $v_0 + v_c \leq 60$ ,  $v_c \in [10, 20, 30, 40, 50, 60]$ . The resulting sequence  $\mathbf{V}_{v_0:v_0+v_c}$  is encoded through a lightweight, randomly-initialized Hiera vision transformer (Ryali et al., 2023), followed by a linear projection to our model dimension,  $d_M$ , producing spatiotemporal embeddings  $\tilde{\mathbf{V}} \in \mathbb{R}^{h' \times w' \times v'_c \times d_M}$ , where  $h'$ ,  $w'$ , and  $v'_c$  result from the stride of the Hiera module.

Table 1: **Scaling variants of OmniMouse.**  $L$ : multi-modal transformer layers;  $d_m$ : model dimension;  $h$ : number of attention heads;  $d_e$ : dimensions of all embeddings;  $p_L$ : multi-modal transformer layer parameters;  $p_M$ : model parameters (excluding neuronal embeddings);  $p_N$ : all neuronal, session, and animal parameters;  $p_T$ : total parameters;  $S$ : sequence length.

Model	$L$	$d_m$	$h$	$d_e$	$p_L$	$p_M$	$p_N$	$p_T$	$S$
OmniMouse-1M	2	256	4	256	1.7M	6M	779M	885M	4096
OmniMouse-5M	6	256	8	256	5.1M	10.4M	779M	891M	4096
OmniMouse-20M	6	512	8	256	19.1M	29.1M	779M	810M	4096
OmniMouse-80M	12	768	12	256	88M	115M	779M	894M	4096
OmniMouse-300M	24	1024	16	256	308M	348M	779M	1.1B	4096

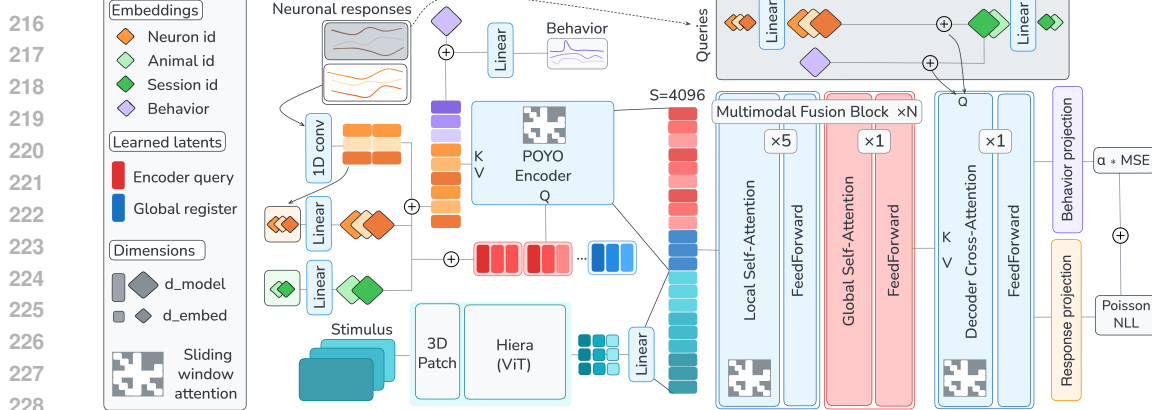


**Figure 3: Model architecture.** We tokenize the visual stimuli with a Hiera encoder, behavior via a shared linear projection with specific embeddings, and responses following POYO+ (Azabou et al., 2025). All tokens are concatenated and processed by transformer blocks, with behavior and responses decoded through cross-attention.

For *neural responses*, during training we randomly sample  $S = 4096$  neurons from population  $P$ . From these we select  $P_{target} = 3072$  neurons whose final second of activity serves as our prediction target. From the remaining data, we collect activity sequences of each neuron’s *unmasked* samples. For OmniMouse, we developed a novel and a flexible neural activity masking scheme that allows for any combination of input masks, down to single-neuron single-sample precision (Fig. 5). The scheme defines a *population prefix* — activity from the population before the last 30 samples — and a *population context* — activity from neurons not being predicted, possibly overlapping in time with the prediction targets. To avoid inflated scores from upsampling artifacts, a gap of at least 0.17 seconds (5 samples) was enforced between the *prefix* and the prediction target. To tokenize the unmasked activity, we apply a strided 1D-convolution to each neuron’s sequence and concatenate the outputs, creating a unified sequence of activity embeddings,  $\tilde{\mathbf{X}} \in \mathbb{R}^{S*T \times d_M}$ , where  $T$  is the number of strides per neuron sequence. Following POYO (Azabou et al., 2023), we add learned identity embeddings for each neuron, session, and animal to the activity features. We use a smaller dimension,  $d_e$ , for these embeddings and up-project to  $d_M$  in order to reduce the number of parameters learned per-neuron.

For *behavior*, we either fully mask or fully unmask the input. When unmasked, we use a shared linear to project the traces along the temporal dimension and add learned channel-specific embeddings (as well as the session/animal embeddings), yielding  $\tilde{\mathbf{B}} \in \mathbb{R}^{5 \times d_M}$ , for 5 behavior channels.

Each token also maintains its timestamp for positional encoding in the input sequence.

**Model architecture.** After tokenization, we concatenate activity and behavior,  $[\tilde{\mathbf{X}}, \tilde{\mathbf{B}}]$ , and encode using cross-attention with a repeated set of learned latents (Azabou et al., 2023),  $\tilde{\mathbf{Z}} \in \mathbb{R}^{M*N \times d_M}$ , ( $M$  unique latents and  $N$  repeats, each repeat with a unique timestamp evenly spaced across the context window), generally reducing the number of input tokens by  $\sim 10$ . Within the cross-attention block, we implement *local sliding-window attention*, where latent features only attend to response / behavior features within a fixed temporal window. We also append  $g = 256$  “global registers” (Darce et al., 2023),  $\mathbf{G} \in \mathbb{R}^{g \times d_M}$  which always attend to the entire sequence.

Then we concatenate the cross-attention output and video features,  $[\tilde{\mathbf{Z}}, \tilde{\mathbf{V}}$ ], and pass the sequence to a series of  $L$  multi-modal transformer layers (Tab. 1). We interleave local attention (with a sliding-window mask), and global attention blocks at a ratio of 5 : 1 (Fig. 3).

To decode neuronal activity and behavior, we again use cross-attention, using fused multi-modal features as keys  $K$  and values  $V$  (Fig. 3). Query construction mirrors the input construction: for samples in the response prediction

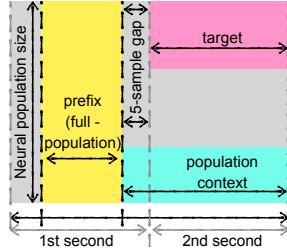


**Figure 4: Neuronal response masking.** We introduce a flexible scheme that supports arbitrary input masks, down to single-neuron, single-sample, and single-frame precision.

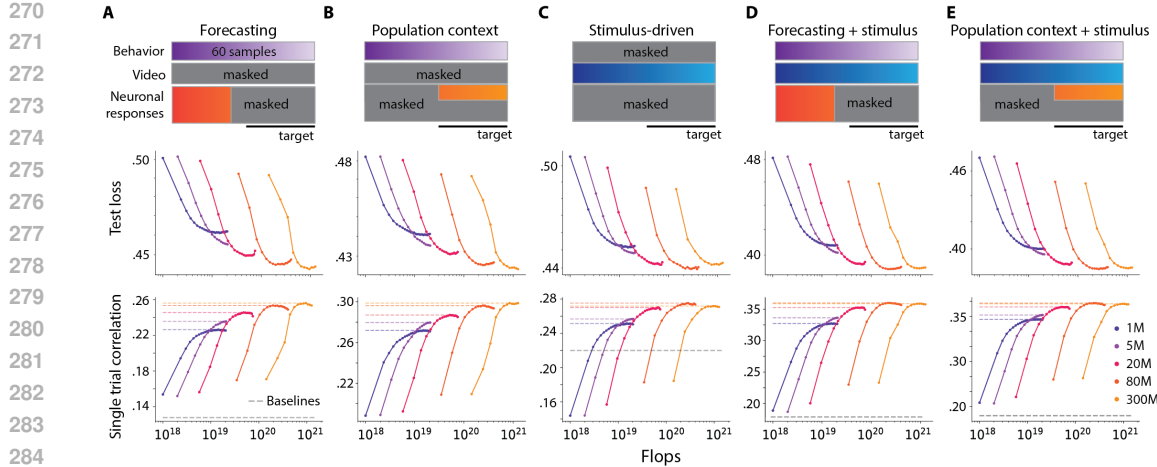


**Figure 5: Task-specific performance gains with model scaling.** Top row: masking schema. Middle row: Test loss. Bottom row: single-trial correlation on seven SENSORIUM 2022 & 2023 mice. Both loss and correlations are computed on the final test split for natural video. **A.** Forecasting, prefix = 25 samples. **B.** Population context, context = 256 neurons. **C.** Stimulus-driven. **D.** Stimulus-conditioned forecasting, prefix = 25 samples. **E.** Stimulus-conditioned population context, context = 256 neurons.

target, we create a sequence of embeddings using the same learned neuron, animal, and session identity embeddings, with only the activity embedding left out. Each query also maintains a timestamp indicating the position of target sample to be decoded. Similarly, to decode each channel of behavior we use the same channel embeddings used for the behavior input. Note, during training behavior is always masked in the input if it is also a prediction target. Finally, the outputs of the decoder cross-attention block for each modality are routed to modality-specific linear readouts, projecting from  $d_M$  back to the original dimensionality. All attentions use RoPE (Su et al., 2024) to encode relative timing between features, both within and across modalities, as well as recent best practices including: RMSNorm pre-normalization layers, query-key normalization, and gated SiLU feed-forward networks (Shazeer, 2020; OLMo et al., 2024; Yang et al., 2025; Biderman et al., 2023).

**Training.** We trained our model to predict both neuronal responses and behavioral traces, using Poisson loss (averaged across neurons) for neural encoding and mean squared error (MSE) loss for behavior decoding. We used 119 masking configurations App. C.4.1) during training, varying which modalities were fully or partially masked as well as the amount and duration of neuronal context. To balance the two objectives, the behavioral loss is down-weighted by a factor of 0.1 so that its scale matches the magnitude of the Poisson loss. For our scaling experiments, we trained models on either the complete dataset of 323 sessions or constructed collections (8, 16, 32, 64 sessions) to study data scaling effects. These nested collections were designed so that larger collections always contained all sessions from smaller ones, ensuring consistent evaluation (see below for evaluation details). We followed Hu et al. (2024); Wen et al. (2024); Hägele et al. (2024) and trained our model with warmup followed by a constant learning rate for at least 250k steps, corresponding to 500B tokens. We then restart training from intermediate checkpoints every 20k steps, and use inverse square root learning rate decay for 10k steps.

## 5 UNIFIED EVALUATION FRAMEWORK

All scaling experiments use a standardized evaluation protocol on the same mice to ensure fair comparison across models, baselines, and conditions. We chose seven mice (*evaluation mice*) comprised of five publicly available datasets from SENSORIUM 2023 and two test mice from SENSORIUM 2022. For all analyses, we use the held-out set provided by these datasets. We evaluate five regimes of response prediction (Fig. 5) as well as behavior decoding (Fig. 6):

**Forecasting** conditions predictions on the past activity of the entire population and 40 frames of behavior. We always predict the last second (30 samples) within each two-second batch, using the first 25 frames of the batch as context. Since NDT-based models (Ye & Pandarinath, 2021) dominate

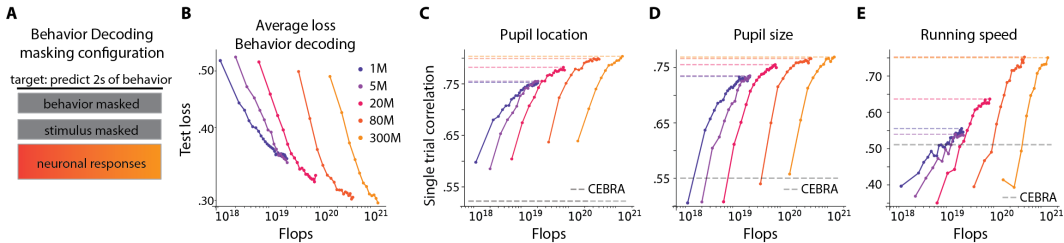


Figure 6: **Behavior decoding scales with model size.** **A.** Masking for behavior decoding. **B.** Decoding loss averaged over all behavioral variables. **C.** Pupil center: correlations computed separately for  $x$  and  $y$ , then averaged. **D.** Pupil size and its derivative: correlations trace, then averaged. **E.** Running speed: correlation with ground truth.

in the forecasting literature, we use IBL (Zhang et al., 2024), a variant of NDT trained with multiple masking strategies similar to ours, as a baseline.

**Population context** conditions predictions on  $N = 256$  other simultaneously recorded neurons and 40 frames of behavior. As in the forecasting regime, we predict the last second of each batch and evaluate performance on this interval. This setting assesses how much of the trial-to-trial variability can be explained by simultaneously recorded neurons.

**Stimulus-driven** conditions predictions on two seconds of video and predicts activity for all neurons in the batch. We provide two seconds of input and evaluate predictions on the final second of neural activity. SENSORIUM 2023 (Turishcheva et al., 2024) establishes a strong baseline for this setting. **Stimulus-conditioned forecasting** is identical to forecasting, except that the full 2 seconds of video are also provided as input. We used Schmidt et al. (2025) as a baseline model, which also conditions on neurons, video and behavior.

**Stimulus-conditioned population context** is identical to population context, except that the full 2 seconds of video are also provided as input. Again, Schmidt et al. (2025) was used as a baseline. **Behavior prediction** conditions on the activity of all neurons (without video) and simultaneously predicts all behavioral traces (i.e. pupil size, pupil location and running speed). CEBRA (Schneider et al., 2023) is used as a baseline for this regime.

We train all state-of-the-art baselines on the collection of eight mice, used in our smallest data-scaling experiment (Fig. 7) to reduce computational cost. Implementation details and hyperparameters for each baseline are provided in App. C. Consistent with SENSORIUM 2022/2023 competitions, we use single-trial correlation as an evaluation metric. Additionally we evaluate our model on the SENSORIUM 2023 competition test set, which allows direct comparison against the state of the art model of predicting mouse visual cortex responses from video stimuli. We use OmniMouse-80M, freeze the entire model, and train only the neuron and animal embeddings using the released training data of five mice provided by the competition.

Table 2: **OmniMouse is state of the art on all tasks.** Correlations were computed across all neurons, except in population context tasks, which used a held-out 50%. For all mice we used final test set, with in-domain (natural stimuli) split for SENSORIUM 2023 mice. Forecasting used 25 frames; population masking 256 neurons.

Prediction task	Baseline	Baseline score ↑	OmniMouse-300M (ours) ↑
Forecasting	IBL (Zhang et al., 2024)	0.12	<b>0.26</b>
Forecasting + stimulus	Latent Model (Schmidt et al., 2025)	0.18	<b>0.36</b>
Stimulus driven	Sensorium 2023 Baseline (Turishcheva et al., 2024)	0.23	<b>0.28</b>
Population context	N.A.	X	<b>0.30</b>
Population context + stimulus	Latent Model (Schmidt et al., 2025)	0.16	<b>0.37</b>
Behavior decoding:			
Pupil location	CEBRA (Schneider et al., 2023)	0.52	<b>0.81</b>
Pupil size	CEBRA (Schneider et al., 2023)	0.55	<b>0.76</b>
Running speed	CEBRA (Schneider et al., 2023)	0.51	<b>0.75</b>
Stimulus driven (attentive probe):			
Sensorium 2023 competition	DwiseNeuro (Turishcheva et al., 2024)	0.30	<b>0.34</b>

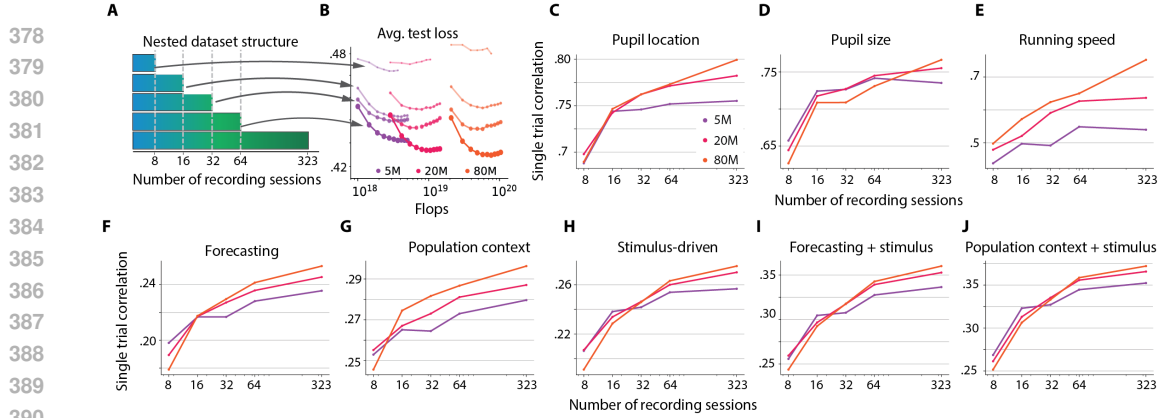


**Figure 7: Scaling data improves model performance.** **A.** Nested datasets structure. **B.** Test loss for different model and data sizes, averaged across all response prediction tasks. **C-K.** Performance improvements when scaling dataset from 8 to 323 sessions: **C.** Pupil center location. **D.** Pupil size and rate of pupil change. **E.** Running speed. **F.** Forecasting, prefix = 25 samples. **J.** Population context, context = 256 neurons. **H.** Stimulus-driven. **I.** Stimulus-conditioned forecasting, prefix = 25 samples. **K.** Stimulus-conditioned population context, context = 256 neurons.

## 6 RESULTS: THE BENEFITS OF SCALING

**Current neuronal-predictive models are not compute- or parameter-limited.** Because collecting neuronal data is costly, we first asked if existing models are already limited by compute or parameters, or if more data would still improve performance. To answer this question, we trained models on all 323 sessions while scaling width and depth as in Tab. 1. We evaluated five neuronal response masking strategies (Fig. 5, top row): two based on response dynamics (forecasting and population context), two analogous variants that additionally condition on video (video-conditioned forecasting and video-conditioned population context), and one stimulus-driven strategy (video & behavior). For each strategy, models ranged from 1M to 300M parameters, and we tracked both test loss and single-trial correlation as a function of total compute (model FLOPs, excluding FLOPS of neuron-specific parameters). Performance improved across all neuronal prediction tasks as model size increased up to 80M parameters (Fig. 5). Beyond this point, gains were minimal, as loss curves saturated or overfit, indicating that current models are data-limited rather than compute- or parameter-limited.

**OmniMouse-300M achieves state-of-the-art performance across all tasks.** Our large-scale model outperforms all baselines across six evaluation regimes for both response and behavior prediction (Tab. 2). We establish new state-of-the-art results in stimulus-driven response prediction and achieve the highest score to date on the Sensorium 2023 competition (Tab. 2)—remarkably, with OmniMouse frozen and only neuron-specific parameters trained.

**Behavior prediction shows the most promising scaling dynamics on the available data.** To characterize the scaling of behavior prediction, we used the same models and evaluated their ability to predict pupil location, pupil size, and running speed from neuronal activity only (Fig. 6). Across all three settings, performance improved smoothly with compute budget, reminiscent of classic scaling-law behavior. Larger models consistently achieved higher single-trial correlations, albeit with an indication of saturation at the largest scale tested. Note, though, that training was stopped to avoid overfitting for the response prediction task. The models had not yet fully converged for the behavior prediction task and longer training could have improved performance further even on the largest model. OmniMouse not only matches, but surpasses the performance of all strong baselines such as CEBRA, particularly for running speed prediction, where correlation improves by over 0.15% relative to the baseline. These results show that behavioral prediction continues to improve with model scaling and may benefit from further increases in capacity.

**Scaling dataset size improves performance.** To study how dataset size affects performance, we trained three model sizes – 5M, 20M, and 80M – on nested collections of 8, 16, 32, 64, and 323 sessions such that the larger collections are supersets of the smaller ones (Fig. 7A). For evaluation, we test the model on the same held-out test set of the same seven mice that were contained in all collections (Fig. 7C–J). In all cases, performance improved with the number of sessions, exhibiting

predictable data-scaling trends. Larger models consistently benefited more from additional data. The larger models required a minimum size of the training set to outperform the smaller models and the performance gap widened as the dataset increased in size. Behavior decoding benefited the most from data scaling (Fig. 7C–E), showing no saturation and large performance differences between 5M and 80M models. For responses, the strongest gains were observed for tasks that included video input (Fig. 7C–E), where the 80M models continued to improve even beyond 100 sessions, suggesting that they remained data-limited rather than capacity-limited. The *forecasting* and *population context* showed bigger benefits from scaling of both data and model sizes. The gaps between 20M and 80M models (Fig. 7A, B) increased faster compared to the tasks with video input, which could indicate a lack of diversity of the visual stimuli in our dataset. Overall, these results highlight that scaling both model size and data quantity is synergistic and necessary to approach peak predictive performance.

**OmniMouse enables systematic evaluation of how neuronal context shapes predictive performance.** Lastly, we assessed the model’s generalization by testing on masking conditions not seen during training, varying neuronal history duration (10–25 frames) and population context size (16–2048 neurons). Performance scaled smoothly with additional context demonstrating that OmniMouse learns generalizable representations that enables systematic analyses of contextual contributions to neural variability (see Fig. S1, and App. A).

## 7 DISCUSSION

In this work we introduce OmniMouse, a multi-modal, multi-task foundation model of mouse visual cortex that integrates neural activity, video, and behavior across animals. A single model achieves state-of-the-art performance on diverse tasks – predicting neural responses from visual stimuli, forecasting activity and decoding behavior. Trained on the largest neural dataset to date (3.3M neurons, 78 mice, 323 sessions), OmniMouse enables systematic study of scaling in brain models.

Our motivation for studying scaling laws is practical: if brain models are to become foundation models for neuroscience, it is essential to ask whether current data can sustain scaling. Despite using naturalistic movies and images, we find that performance saturates with model size, suggesting data – not compute – as the limiting factor. Even in the relatively simple mouse visual system, richer tasks, more varied stimuli, and larger-scale recordings are needed to support continued scaling. At the same time, relatively sparse sampling already yields strong models: with 60,000 neurons from just eight mice, predictive accuracy is high, likely due to redundancy in neural codes. Additional gains from larger datasets appear modest, paralleling language and vision models – yet in those domains, such small improvements have triggered phase transitions to qualitatively new abilities. By analogy, richer neuroscience data may similarly unlock new capabilities in brain models, revealing deeper principles of neural computation.

**Limitations.** Our work has several limitations. First, OmniMouse parameters scale linearly with the number of neurons, as it learns per-neuron embeddings. This makes training computationally prohibitively expensive may limit scaling to even larger datasets. Second, large-scale transformers remain difficult to interpret, and like deep learning models, they are prone to optimization issues and overparameterization, which constrain the biological insights that can be drawn. Furthermore, the behavioral data present in our data is limited to spontaneous activity and it is thus unclear if this approach can transfer to more complex behaviors.

**Future work.** Future work could extend to stimulus decoding (Benchetrit et al., 2023; Bauer et al., 2024; Zhu et al., 2025) and more precise study of training dynamics of modality interactions and multi-task learning to improve the masking recipe. Beyond calcium imaging in mouse visual cortex, models could integrate other data types such as electrophysiological recordings, diverse animal species, and more multi-modal stimuli such as audio. Alternatively, one could test generalization of the existing model across new tasks, stimuli, and species via (semi) closed-loop in-silico experiments (Ustyuzhaninov et al., 2022; Li et al., 2025), potentially finding biological insights about neuronal functional properties as in Walker et al. (2019); Li et al. (2025). Finally, jointly modeling visual input, neuronal responses, and behavior enables analysis of spontaneous and evoked activity (Stringer et al., 2019), revealing how brain state shapes sensory processing and core principles of computation.

486 REFERENCES  
487

- 488 Josh Abramson, Jonas Adler, Jack Dunger, Richard Evans, Tim Green, Alexander Pritzel, Olaf Ron-  
489 neberger, Lindsay Willmore, Andrew J Ballard, Joshua Bambrick, et al. Accurate structure pre-  
490 diction of biomolecular interactions with alphafold 3. *Nature*, 630(8016):493–500, 2024.
- 491 Armen Aghajanyan, Lili Yu, Alexis Conneau, Wei-Ning Hsu, Karen Hambardzumyan, Susan Zhang,  
492 Stephen Roller, Naman Goyal, Omer Levy, and Luke Zettlemoyer. Scaling laws for generative  
493 mixed-modal language models. In *International Conference on Machine Learning*, pp. 265–279.  
494 PMLR, 2023.
- 495 Dora Angelaki, Brandon Benson, Julius Benson, Daniel Birman, Niccolò Bonacchi, Kénia  
496 Bougrova, Sebastian A Bruijns, Matteo Carandini, Joana A Catarino, et al. A brain-wide map  
497 of neural activity during complex behaviour. *Nature*, 645(8079):177–191, 2025.
- 498 Ján Antolík, Sonja B Hofer, James A Bednar, and Thomas D Mrsic-Flogel. Model constrained by  
499 visual hierarchy improves prediction of neural responses to natural scenes. *PLoS computational  
500 biology*, 12(6):e1004927, 2016.
- 501 502 Richard Antonello, Aditya Vaidya, and Alexander Huth. Scaling laws for language encoding models  
503 in fmri. *Advances in Neural Information Processing Systems*, 36:21895–21907, 2023.
- 504 505 Antonis Antoniades, Yiyi Yu, Joseph Canzano, William Wang, and Spencer LaVere Smith. Neu-  
506 roformer: Multimodal and multitask generative pretraining for brain data, 2024. URL <https://arxiv.org/abs/2311.00136>.
- 507 508 Mehdi Azabou, Vinam Arora, Venkataramana Ganesh, Ximeng Mao, Santosh Nachimuthu, Michael  
509 Mendelson, Blake Richards, Matthew Perich, Guillaume Lajoie, and Eva Dyer. A unified, scalable  
510 framework for neural population decoding. *Advances in Neural Information Processing Systems*,  
511 36:44937–44956, 2023.
- 512 513 Mehdi Azabou, Krystal Xuejing Pan, Vinam Arora, Ian Jarratt Knight, Eva L Dyer, and Blake Aaron  
514 Richards. Multi-session, multi-task neural decoding from distinct cell-types and brain regions. In  
515 *The Thirteenth International Conference on Learning Representations*, 2025.
- 516 517 Mohammad Bashiri, Edgar Walker, Konstantin-Klemens Lurz, Akshay Jagadish, Taliah Muhammad,  
518 Zhiwei Ding, Zhuokun Ding, Andreas Tolias, and Fabian Sinz. A flow-based latent state gener-  
519 ative model of neural population responses to natural images. *Advances in Neural Information  
520 Processing Systems*, 34:15801–15815, 2021.
- 521 Eleanor Batty, Josh Merel, Nora Brackbill, Alexander Heitman, Alexander Sher, Alan Litke,  
522 EJ Chichilnisky, and Liam Paninski. Multilayer recurrent network models of primate retinal gan-  
523 glion cell responses. In *International Conference on Learning Representations*, 2017.
- 524 525 Joel Bauer, Troy W Margrie, and Claudia Clopath. Movie reconstruction from mouse visual cortex  
526 activity. *bioRxiv*, pp. 2024–06, 2024.
- 527 528 Yohann Benchetrit, Hubert Banville, and Jean-Rémi King. Brain decoding: toward real-time recon-  
529 struction of visual perception. *arXiv preprint arXiv:2310.19812*, 2023.
- 530 531 Stella Biderman, Hailey Schoelkopf, Quentin Gregory Anthony, Herbie Bradley, Kyle O’Brien, Eric  
532 Hallahan, Mohammad Aflah Khan, Shivanshu Purohit, Usvsn Sai Prashanth, Edward Raff, Aviya  
533 Skowron, Lintang Sutawika, and Oskar Van Der Wal. Pythia: A suite for analyzing large lan-  
534 guage models across training and scaling. In Andreas Krause, Emma Brunskill, Kyunghyun  
535 Cho, Barbara Engelhardt, Sivan Sabato, and Jonathan Scarlett (eds.), *Proceedings of the 40th  
536 International Conference on Machine Learning*, volume 202 of *Proceedings of Machine Learning  
537 Research*, pp. 2397–2430. PMLR, 23–29 Jul 2023. URL <https://proceedings.mlr.press/v202/biderman23a.html>.
- 538 539 David H Brainard and Spatial Vision. The psychophysics toolbox. *Spatial vision*, 10(4):433–436,  
1997.

- 540 Max F Burg, Santiago A Cadena, George H Denfield, Edgar Y Walker, Andreas S Tolias, Matthias  
 541 Bethge, and Alexander S Ecker. Learning divisive normalization in primary visual cortex. *PLOS*  
 542 *Computational Biology*, 17(6):e1009028, 2021.
- 543 Santiago A. Cadena, George H. Denfield, Edgar Y. Walker, Leon A. Gatys, Andreas S. Tolias,  
 544 Matthias Bethge, and Alexander S. Ecker. Deep convolutional models improve predictions of  
 545 macaque v1 responses to natural images. *PLOS Computational Biology*, 15(4):e1006897, April  
 546 2019. doi: 10.1371/journal.pcbi.1006897.
- 547 Charles F Cadieu, Ha Hong, Daniel L K Yamins, Nicolas Pinto, Diego Ardila, Ethan A Solomon,  
 548 Najib J Majaj, and James J DiCarlo. Deep neural networks rival the representation of primate IT  
 549 cortex for core visual object recognition. *PLoS Comput. Biol.*, 10(12):e1003963, 2014.
- 550 Salvatore Calcagno, Isaak Kavasidis, Simone Palazzo, Marco Brondi, Luca Sità, Giacomo Turri,  
 551 Daniela Giordano, Vladimir R. Kostic, Tommaso Fellin, Massimiliano Pontil, and Concetto  
 552 Spampinato. Quantformer: Learning to quantize for neural activity forecasting in mouse visual  
 553 cortex, 2024. URL <https://arxiv.org/abs/2412.07264>.
- 554 Josue Ortega Caro, Antonio H de O Fonseca, Christopher Averill, Syed A Rizvi, Matteo Rosati,  
 555 James L Cross, Prateek Mittal, Emanuele Zappala, Daniel Levine, Rahul M Dhodapkar, et al.  
 556 Brainlm: A foundation model for brain activity recordings. *bioRxiv*, pp. 2023–09, 2023.
- 557 Team Chameleon. Chameleon: Mixed-modal early-fusion foundation models, 2024. URL  
 558 <https://arxiv.org/abs/2405.09818>, 9(8), 2024.
- 559 Geeling Chau, Christopher Wang, Sabera Talukder, Vighnesh Subramaniam, Saraswati Soedarmadji,  
 560 Yisong Yue, Boris Katz, and Andrei Barbu. Population transformer: Learning population-level  
 561 representations of neural activity. *ArXiv*, pp. arXiv–2406, 2024.
- 562 Yuqi Chen, Kan Ren, Kaitao Song, Yansen Wang, Yifan Wang, Dongsheng Li, and Lili Qiu. Eeg-  
 563 former: Towards transferable and interpretable large-scale eeg foundation model. *arXiv preprint*  
 564 *arXiv:2401.10278*, 2024.
- 565 BR Cowley and JW Pillow. High-contrast "gaudy" images improve the training of deep neural net-  
 566 work models of visual cortex. In H. Larochelle, M. Ranzato, R. Hadsell, M.F. Balcan, and H. Lin  
 567 (eds.), *Advances in Neural Information Processing Systems* 33, pp. 21591–21603. Curran Asso-  
 568 ciates, Inc., 2020.
- 569 Richard Csaky, Mats WJ van Es, Oiwi Parker Jones, and Mark Woolrich. Foundational gpt model  
 570 for meg. *arXiv preprint arXiv:2404.09256*, 2024.
- 571 Wenhui Cui, Woojae Jeong, Philipp Thölke, Takfarinas Medani, Karim Jerbi, Anand A Joshi, and  
 572 Richard M Leahy. Neuro-gpt: Towards a foundation model for eeg. In *2024 IEEE International*  
 573 *Symposium on Biomedical Imaging (ISBI)*, pp. 1–5. IEEE, 2024.
- 574 Timothée Darcet, Maxime Oquab, Julien Mairal, and Piotr Bojanowski. Vision transformers need  
 575 registers. *arXiv preprint arXiv:2309.16588*, 2023.
- 576 Stéphane d’Ascoli, Jérémie Rapin, Yohann Benchetrit, Hubert Banville, and Jean-Rémi King.  
 577 Tribe: Trimodal brain encoder for whole-brain fmri response prediction. *arXiv preprint*  
 578 *arXiv:2507.22229*, 2025.
- 579 Saskia E. J. de Vries, Jerome A. Lecoq, Michael A. Buice, Peter A. Groblewski, Gabriel K. Ocker,  
 580 Michael Oliver, David Feng, Nicholas Cain, Peter Ledochowitsch, Daniel Millman, Kate Roll,  
 581 Marina Garrett, Tom Keenan, Leonard Kuan, Stefan Mihalas, Shawn Olsen, Carol Thompson,  
 582 Wayne Wakeman, Jack Waters, Derric Williams, Chris Barber, Nathan Berbesque, Brandon Blan-  
 583 chard, Nicholas Bowles, Shiella D. Caldejon, Linzy Casal, Andrew Cho, Sissy Cross, Chinh  
 584 Dang, Tim Dolbeare, Melise Edwards, John Galbraith, Nathalie Gaudreault, Terri L. Gilbert,  
 585 Fiona Griffin, Perry Hargrave, Robert Howard, Lawrence Huang, Sean Jewell, Nika Keller, Ulf  
 586 Knoblich, Josh D. Larkin, Rachael Larsen, Chris Lau, Eric Lee, Felix Lee, Arielle Leon, Lu Li,  
 587 Fuhui Long, Jennifer Luviano, Kyla Mace, Thuyanh Nguyen, Jed Perkins, Miranda Robertson,  
 588 Sam Seid, Eric Shea-Brown, Jianghong Shi, Nathan Sjoquist, Cliff Slaughterbeck, David Sulli-  
 589 van, Ryan Valenza, Casey White, Ali Williford, Daniela M. Witten, Jun Zhuang, Hongkui Zeng,

- 594 Colin Farrell, Lydia Ng, Amy Bernard, John W. Phillips, R. Clay Reid, and Christof Koch. A  
 595 large-scale standardized physiological survey reveals functional organization of the mouse visual  
 596 cortex. *Nature Neuroscience*, 23(1):138–151, December 2019. doi: 10.1038/s41593-019-0550-9.  
 597 URL <https://doi.org/10.1038/s41593-019-0550-9>.
- 598 Zhiwei Ding, Dat T. Tran, Kayla Ponder, Zhuokun Ding, Rachel Froebe, Lydia Ntanavara, Paul G.  
 599 Fahey, Erick Cobos, Luca Baroni, Maria Diamantaki, Eric Y. Wang, Andersen Chang, Stelios Pa-  
 600 padopoulos, Jiakun Fu, Taliah Muhammad, Christos Papadopoulos, Santiago A. Cadena, Alexan-  
 601 dros Evangelou, Konstantin Willeke, Fabio Anselmi, Sophia Sanborn, Jan Antolik, Emmanouil  
 602 Froudarakis, Saumil Patel, Edgar Y. Walker, Jacob Reimer, Fabian H. Sinz, Alexander S. Ecker,  
 603 Katrin Franke, Xaq Pitkow, and Andreas S. Tolias. Bipartite invariance in mouse primary visual  
 604 cortex. *bioRxiv*, 2025a. doi: 10.1101/2023.03.15.532836. URL <https://www.biorxiv.org/content/early/2025/04/19/2023.03.15.532836>.
- 605 Zhuokun Ding, Paul G Fahey, Stelios Papadopoulos, Eric Y Wang, Brendan Celii, Christos Pa-  
 606 padopoulos, Andersen Chang, Alexander B Kunin, Dat Tran, Jiakun Fu, et al. Functional con-  
 607 nectomics reveals general wiring rule in mouse visual cortex. *Nature*, 640(8058):459–469, 2025b.
- 608 Zijian Dong, Ruilin Li, Yilei Wu, Thuan Tinh Nguyen, Joanna Chong, Fang Ji, Nathanael Tong,  
 609 Christopher Chen, and Juan Helen Zhou. Brain-jepa: Brain dynamics foundation model with  
 610 gradient positioning and spatiotemporal masking. *Advances in Neural Information Processing  
 Systems*, 37:86048–86073, 2024.
- 611 Yu Duan, Hamza Tahir Chaudhry, Misha B Ahrens, Christopher D Harvey, Matthew G Perich, Karl  
 612 Deisseroth, and Kanaka Rajan. Poco: Scalable neural forecasting through population conditioning.  
 613 *arXiv preprint arXiv:2506.14957*, 2025.
- 614 Alexander S. Ecker, Fabian H. Sinz, Emmanouil Froudarakis, Paul G. Fahey, Santiago A. Cadena,  
 615 Edgar Y. Walker, Erick Cobos, Jacob Reimer, Andreas S. Tolias, and Matthias Bethge. A rotation-  
 616 equivariant convolutional neural network model of primary visual cortex. *arXiv*, 2018.
- 617 Paul G Fahey, Taliah Muhammad, Cameron Smith, Emmanouil Froudarakis, Erick Cobos, Jiakun  
 618 Fu, Edgar Y Walker, Dimitri Yatsenko, Fabian H Sinz, Jacob Reimer, et al. A global map of  
 619 orientation tuning in mouse visual cortex. *BioRxiv*, pp. 745323, 2019.
- 620 Emmanouil Froudarakis, Philipp Berens, Alexander S Ecker, R James Cotton, Fabian H Sinz, Dimitri  
 621 Yatsenko, Peter Saggau, Matthias Bethge, and Andreas S Tolias. Population code in mouse V1  
 622 facilitates readout of natural scenes through increased sparseness. *Nat. Neurosci.*, 17(6):851–857,  
 623 June 2014.
- 624 Marina E Garrett, Ian Nauhaus, James H Marshel, and Edward M Callaway. Topography and areal  
 625 organization of mouse visual cortex. *J. Neurosci.*, 34(37):12587–12600, September 2014.
- 626 Andrea Giovannucci, Johannes Friedrich, Pat Gunn, Jérémie Kalfon, Brandon L Brown, Sue Ann  
 627 Koay, Jiannis Taxidis, Farzaneh Najafi, Jeffrey L Gauthier, Pengcheng Zhou, et al. Caiman an  
 628 open source tool for scalable calcium imaging data analysis. *elife*, 8:e38173, 2019.
- 629 Abdulkadir Gokce and Martin Schrimpf. Scaling laws for task-optimized models of the primate  
 630 visual ventral stream. *arXiv preprint arXiv:2411.05712*, 2024.
- 631 Alexander Hägele, Elie Bakouch, Atli Kosson, Loubna Ben Allal, Leandro Von Werra, and Martin  
 632 Jaggi. Scaling laws and compute-optimal training beyond fixed training durations. In A. Globerson,  
 633 L. Mackey, D. Belgrave, A. Fan, U. Paquet, J. Tomczak, and C. Zhang (eds.), *Advances  
 634 in Neural Information Processing Systems*, volume 37, pp. 76232–76264. Curran Associates,  
 635 Inc., 2024. URL [https://proceedings.neurips.cc/paper\\_files/paper/2024/file/8b970e15a89bf5d12542810df8ae8fc-Paper-Conference.pdf](https://proceedings.neurips.cc/paper_files/paper/2024/file/8b970e15a89bf5d12542810df8ae8fc-Paper-Conference.pdf).
- 636 Jordan Hoffmann, Sebastian Borgeaud, Arthur Mensch, Elena Buchatskaya, Trevor Cai, Eliza Rutherford,  
 637 Diego de Las Casas, Lisa Anne Hendricks, Johannes Welbl, Aidan Clark, et al. Training  
 638 compute-optimal large language models. *arXiv preprint arXiv:2203.15556*, 2022.
- 639 Shengding Hu, Yuge Tu, Xu Han, Chaoqun He, Ganqu Cui, Xiang Long, Zhi Zheng, Yewei Fang,  
 640 Yuxiang Huang, Weilin Zhao, et al. Minicpm: Unveiling the potential of small language models  
 641 with scalable training strategies. *arXiv preprint arXiv:2404.06395*, 2024.

- 648 Linxing Preston Jiang, Shirui Chen, Emmanuel Tanumihardja, XiaoChuang Han, Weijia Shi, Eric  
 649 Shea-Brown, and Rajesh PN Rao. Data heterogeneity limits the scaling effect of pretraining neural  
 650 data transformers. [bioRxiv](#), pp. 2025–05, 2025.
- 651 Wei-Bang Jiang, Li-Ming Zhao, and Bao-Liang Lu. Large brain model for learning generic repre-  
 652 sentations with tremendous eeg data in bci. [arXiv preprint arXiv:2405.18765](#), 2024.
- 653 Xuan Kan, Wei Dai, Hejie Cui, Zilong Zhang, Ying Guo, and Carl Yang. Brain network transformer.  
 654 [Advances in Neural Information Processing Systems](#), 35:25586–25599, 2022.
- 655 Jared Kaplan, Sam McCandlish, Tom Henighan, Tom B Brown, Benjamin Chess, Rewon Child, Scott  
 656 Gray, Alec Radford, Jeffrey Wu, and Dario Amodei. Scaling laws for neural language models.  
 657 [arXiv preprint arXiv:2001.08361](#), 2020.
- 658 Andrej Karpathy, George Toderici, Sanketh Shetty, Thomas Leung, Rahul Sukthankar, and Li Fei-  
 659 Fei. Large-Scale video classification with convolutional neural networks. In [2014 IEEE](#)  
 660 [Conference on Computer Vision and Pattern Recognition](#), pp. 1725–1732, June 2014.
- 661 William F Kindel, Elijah D Christensen, and Joel Zylberberg. Using deep learning to probe the neural  
 662 code for images in primary visual cortex. [Journal of vision](#), 19(4):29–29, 2019.
- 663 Mario Kleiner, David Brainard, and Denis Pelli. What's new in psychtoolbox-3? 2007.
- 664 David Klindt, Alexander S Ecker, Thomas Euler, and Matthias Bethge. Neural system identification  
 665 for large populations separating “what” and “where”. [Advances in neural information processing](#)  
 666 [systems](#), 30, 2017.
- 667 Demetres Kostas, Stephane Aroca-Ouellette, and Frank Rudzicz. Bendr: Using transformers and a  
 668 contrastive self-supervised learning task to learn from massive amounts of eeg data. [Frontiers in](#)  
 669 [Human Neuroscience](#), 15:653659, 2021.
- 670 Trung Le and Eli Shlizerman. Stndt: Modeling neural population activity with spatiotemporal trans-  
 671 formers. [Advances in Neural Information Processing Systems](#), 35:17926–17939, 2022.
- 672 Bryan M Li, Isabel M Cornacchia, Nathalie L Rochefort, and Arno Onken. V1t: large-scale mouse  
 673 v1 response prediction using a vision transformer. [arXiv preprint arXiv:2302.03023](#), 2023.
- 674 Bryan M Li, Wolf De Wulf, Danai Katsanevaki, Arno Onken, and Nathalie LI Rochefort. Movie-  
 675 trained transformer reveals novel response properties to dynamic stimuli in mouse visual cortex.  
 676 [bioRxiv](#), 2025. doi: 10.1101/2025.09.16.676524. URL <https://www.biorxiv.org/content/early/2025/09/17/2025.09.16.676524>.
- 677 Yamin Li, Ange Lou, Ziyuan Xu, Shengchao Zhang, Shiyu Wang, Dario Englot, Soheil Kolouri,  
 678 Daniel Moyer, Roza Bayrak, and Catie Chang. Neurobolt: Resting-state eeg-to-fmri synthesis  
 679 with multi-dimensional feature mapping. [Advances in Neural Information Processing Systems](#),  
 680 37:23378–23405, 2024.
- 681 Isaac Lin, Tianye Wang, Shang Gao, Shiming Tang, and Tai Sing Lee. Incremental learning and  
 682 self-attention mechanisms improve neural system identification. [arXiv e-prints](#), pp. arXiv–2406,  
 683 2024.
- 684 Konstantin-Klemens Lurz, Mohammad Bashiri, Konstantin Willeke, Akshay Jagadish, Eric Wang,  
 685 Edgar Y. Walker, Santiago A Cadena, Taliah Muhammad, Erick Cobos, Andreas S. Tolias, Alexan-  
 686 der S Ecker, and Fabian H. Sinz. Generalization in data-driven models of primary visual cortex.  
 687 In [International Conference on Learning Representations](#), 2021. URL <https://openreview.net/forum?id=Tp7kI90Htd>.
- 688 Alexander Mathis, Pranav MamiDanna, Kevin M Cury, Taiga Abe, Venkatesh N Murthy, Macken-  
 689 zie Weygandt Mathis, and Matthias Bethge. DeepLabCut: markerless pose estimation of user-  
 690 defined body parts with deep learning. [Nat. Neurosci.](#), 21(9):1281–1289, September 2018.
- 691 Lane T McIntosh, Niru Maheswaranathan, Aran Nayebi, Surya Ganguli, and Stephen A Baccus.  
 692 Deep learning models of the retinal response to natural scenes. [Adv. Neural Inf. Process. Syst.](#), 29  
 693 (Nips):1369–1377, 2016.

- 702 Lu Mi, Trung Le, Tianxing He, Eli Shlizerman, and Uyar Sümbül. Learning time-invariant rep-  
 703 resentations for individual neurons from population dynamics. *Advances in Neural Information  
 704 Processing Systems*, 36:46007–46026, 2023.
- 705 MICrONS Consortium. Functional connectomics spanning multiple areas of mouse visual cortex.  
 706 *Nature*, 640(8058):435–447, April 2025.
- 708 MICrONS Consortium, J Alexander Bae, Mahaly Baptiste, Agnes L Bodor, Derrick Brittain, Joann  
 709 Buchanan, Daniel J Bumbarger, Manuel A Castro, Brendan Celii, Erick Cobos, Forrest Collman,  
 710 Nuno Maçarico da Costa, Sven Dorkenwald, Leila Elabbady, Paul G Fahey, Tim Fliss, Emmanouil  
 711 Froudakis, Jay Gager, Clare Gamlin, Akhilesh Halageri, James Hebditch, Zhen Jia, Chris Jordan,  
 712 Daniel Kapner, Nico Kemnitz, Sam Kinn, Selden Koolman, Kai Kuehner, Kisuk Lee, Kai Li,  
 713 Ran Lu, Thomas Macrina, Gayathri Mahalingam, Sarah McReynolds, Elanine Miranda, Eric  
 714 Mitchell, Shanka Subhra Mondal, Merlin Moore, Shang Mu, Taliah Muhammad, Barak Nehoran,  
 715 Oluwaseun Ogedengbe, Christos Papadopoulos, Stelios Papadopoulos, Saumil Patel, Xaq Pitkow,  
 716 Sergiy Popovych, Anthony Ramos, R Clay Reid, Jacob Reimer, Casey M Schneider-Mizell, H Sebastian  
 717 Seung, Ben Silverman, William Silversmith, Amy Sterling, Fabian H Sinz, Cameron L Smith,  
 718 Shelby Suckow, Zheng H Tan, Andreas S Tolias, Russel Torres, Nicholas L Turner, Edgar Y Walker,  
 719 Tianyu Wang, Grace Williams, Sarah Williams, Kyle Willie, Ryan Willie, William Wong,  
 720 Jingpeng Wu, Chris Xu, Runzhe Yang, Dimitri Yatsenko, Fei Ye, Wenjing Yin, and Szi-Chieh Yu.  
 721 Functional connectomics spanning multiple areas of mouse visual cortex. *bioRxiv*, pp. 721  
 2021.07.28.454025, July 2021.
- 722 Shervin Minaee, Tomas Mikolov, Narjes Nikzad, Meysam Chenaghlu, Richard Socher, Xavier Am-  
 723 atrain, and Jianfeng Gao. Large language models: A survey. *arXiv preprint arXiv:2402.06196*,  
 724 2024.
- 725 M C Morrone, M Tosetti, D Montanaro, A Fiorentini, G Cioni, and D C Burr. A cortical area that  
 726 responds specifically to optic flow, revealed by fMRI. *Nat. Neurosci.*, 3(12):1322–1328, December  
 727 2000.
- 729 Humza Naveed, Asad Ullah Khan, Shi Qiu, Muhammad Saqib, Saeed Anwar, Muhammad Usman,  
 730 Naveed Akhtar, Nick Barnes, and Ajmal Mian. A comprehensive overview of large language  
 731 models. *ACM Transactions on Intelligent Systems and Technology*, 16(5):1–72, 2025.
- 732 Cristopher M Niell and Michael P Stryker. Modulation of visual responses by behavioral state in  
 733 mouse visual cortex. *Neuron*, 65(4):472–479, 2010.
- 735 Team OLMo, Pete Walsh, Luca Soldaini, Dirk Groeneveld, Kyle Lo, Shane Arora, Akshita Bhagia,  
 736 Yuling Gu, Shengyi Huang, Matt Jordan, Nathan Lambert, Dustin Schwenk, Oyvind Tafjord, Taira  
 737 Anderson, David Atkinson, Faeze Brahman, Christopher Clark, Pradeep Dasigi, Nouha Dziri,  
 738 Michal Guerquin, Hamish Ivison, Pang Wei Koh, Jiacheng Liu, Saumya Malik, William Merrill,  
 739 Lester James V Miranda, Jacob Morrison, Tyler Murray, Crystal Nam, Valentina Pyatkin, Aman  
 740 Rangapur, Michael Schmitz, Sam Skjonsberg, David Wadden, Christopher Wilhelm, Michael Wil-  
 741 son, Luke Zettlemoyer, Ali Farhadi, Noah A Smith, and Hannaneh Hajishirzi. 2 OLMo 2 furious.  
 742 December 2024.
- 743 Denis G Pelli. The videotoolbox software for visual psychophysics: transforming numbers into  
 744 movies. *Spatial vision*, 10(4):437–442, 1997.
- 745 Nicolai Petkov and Easwar Subramanian. Motion detection, noise reduction, texture suppression,  
 746 and contour enhancement by spatiotemporal gabor filters with surround inhibition. *Biol. Cybern.*,  
 747 97(5-6):423–439, December 2007.
- 748 AJ Piergiovanni, Isaac Noble, Dahun Kim, Michael S Ryoo, Victor Gomes, and Anelia Angelova.  
 749 Mirasol3b: A multimodal autoregressive model for time-aligned and contextual modalities. In  
 750 *Proceedings of the IEEE/CVF Conference on Computer Vision and Pattern Recognition*, pp.  
 751 26804–26814, 2024.
- 753 Paweł A Pierzchlewicz, Konstantin F Willeke, Arne F Nix, Pavithra Elumalai, Kelli Restivo, Tori  
 754 Shinn, Cate Nealley, Gabrielle Rodriguez, Saumil Patel, Katrin Franke, Andreas S Tolias, and  
 755 Fabian H Sinz. Energy guided diffusion for generating neurally exciting images. In *Advances in  
 Neural Processing Systems (NeurIPS 2023)*, pp. 2023.05.18.541176, May 2023.

- 756 Jacob Reimer, Emmanouil Froudarakis, Cathryn R Cadwell, Dimitri Yatsenko, George H Denfield,  
 757 and Andreas S Tolias. Pupil fluctuations track fast switching of cortical states during quiet wake-  
 758 fulness. *Neuron*, 84(2):355–362, 2014.
- 759
- 760 Olga Russakovsky, Jia Deng, Hao Su, Jonathan Krause, Sanjeev Satheesh, Sean Ma, Zhiheng Huang,  
 761 Andrej Karpathy, Aditya Khosla, Michael Bernstein, Alexander C Berg, and Li Fei-Fei. ImageNet  
 762 large scale visual recognition challenge. *Int. J. Comput. Vis.*, 115(3):211–252, December 2015.
- 763
- 764 Chaitanya Ryali, Yuan-Ting Hu, Daniel Bolya, Chen Wei, Haoqi Fan, Po-Yao Huang, Vaibhav Aggar-  
 765 wal, Arkabandhu Chowdhury, Omid Poursaeed, Judy Hoffman, et al. Hiera: A hierarchical vision  
 766 transformer without the bells-and-whistles. In *International conference on machine learning*, pp.  
 767 29441–29454. PMLR, 2023.
- 768
- 769 Shreya Saha, Ishaan Chadha, et al. Modeling the human visual system: Comparative insights from  
 770 response-optimized and task-optimized vision models, language models, and different readout  
 771 mechanisms. [arXiv preprint arXiv:2410.14031](https://arxiv.org/abs/2410.14031), 2024.
- 772
- 773 Finn Schmidt, Polina Turishcheva, Suhas Shrinivasan, and Fabian H. Sinz. Modeling dynamic neural  
 774 activity by combining naturalistic video stimuli and stimulus-independent latent factors, 2025.  
 775 URL <https://arxiv.org/abs/2410.16136>.
- 776
- 777 Steffen Schneider, Jin Hwa Lee, and Mackenzie Weygandt Mathis. Learnable latent embeddings for  
 778 joint behavioural and neural analysis. *Nature*, 617(7960):360–368, 2023.
- 779
- 780 Noam Shazeer. GLU variants improve transformer. February 2020.
- 781
- 782 Mustafa Shukor, Enrico Fini, Victor Guilherme Turrisi da Costa, Matthieu Cord, Joshua Susskind,  
 783 and Alaaeldin El-Nouby. Scaling laws for native multimodal models. [arXiv preprint  
 784 arXiv:2504.07951](https://arxiv.org/abs/2504.07951), 2025.
- 785
- 786 Fabian Sinz, Alexander S Ecker, Paul Fahey, Edgar Walker, Erick Cobos, Emmanouil Froudarakis,  
 787 Dimitri Yatsenko, Zachary Pitkow, Jacob Reimer, and Andreas Tolias. Stimulus domain transfer  
 788 in recurrent models for large scale cortical population prediction on video. *Advances in neural  
 789 information processing systems*, 31, 2018.
- 790
- 791 Nicholas James Sofroniew, Daniel Flickinger, Jonathan King, and Karel Svoboda. A large field of  
 792 view two-photon mesoscope with subcellular resolution for in vivo imaging. *elife*, 5:e14472, 2016.
- 793
- 794 Carsen Stringer, Marius Pachitariu, Nicholas Steinmetz, Charu Bai Reddy, Matteo Carandini, and  
 795 Kenneth D Harris. Spontaneous behaviors drive multidimensional, brainwide activity. *Science*,  
 796 364(6437):eaav7893, 2019.
- 797
- 798 Jianlin Su, Murtadha Ahmed, Yu Lu, Shengfeng Pan, Wen Bo, and Yunfeng Liu. Roformer: En-  
 799 hanced transformer with rotary position embedding. *Neurocomputing*, 568:127063, 2024.
- 800
- 801 Rahul Thapa, Bryan He, Magnus Ruud Kjaer, Hyatt Moore, Gauri Ganjoo, Emmanuel Mignot, and  
 802 James Zou. Sleepfm: Multi-modal representation learning for sleep across brain activity, ecg and  
 803 respiratory signals. [arXiv preprint arXiv:2405.17766](https://arxiv.org/abs/2405.17766), 2024.
- 804
- 805 Armin Thomas, Christopher Ré, and Russell Poldrack. Self-supervised learning of brain dynam-  
 806 ics from broad neuroimaging data. *Advances in neural information processing systems*, 35:  
 807 21255–21269, 2022.
- 808
- 809 Polina Turishcheva, Paul Fahey, Michaela Vystrčilová, Laura Hansel, Rachel Froebe, Kayla Ponder,  
 810 Yongrong Qiu, Konstantin Willeke, Mohammad Bashiri, Ruslan Baikulov, et al. Retrospective for  
 811 the dynamic sensorium competition for predicting large-scale mouse primary visual cortex activity  
 812 from videos. *Advances in Neural Information Processing Systems*, 37:118907–118929, 2024.
- Ivan Ustyuzhaninov, Max F Burg, Santiago A Cadena, Jiakun Fu, Taliah Muhammad, Kayla Ponder,  
 813 Emmanouil Froudarakis, Zhiwei Ding, Matthias Bethge, Andreas S Tolias, et al. Digital twin re-  
 814 veals combinatorial code of non-linear computations in the mouse primary visual cortex. *BioRxiv*,  
 815 pp. 2022–02, 2022.

- 810 Edgar Y Walker, Fabian H Sinz, Erick Cobos, Taliah Muhammad, Emmanouil Froudarakis, Paul G  
 811 Fahey, Alexander S Ecker, Jacob Reimer, Xaq Pitkow, and Andreas S Tolias. Inception loops dis-  
 812 cover what excites neurons most using deep predictive models. *Nat. Neurosci.*, 22(12):2060–2065,  
 813 December 2019.
- 814 Christopher Wang, Vighnesh Subramaniam, Adam Uri Yaari, Gabriel Kreiman, Boris Katz, Ignacio  
 815 Cases, and Andrei Barbu. Brainbert: Self-supervised representation learning for intracranial  
 816 recordings. *arXiv preprint arXiv:2302.14367*, 2023.
- 817 Eric Y Wang, Paul G Fahey, Zhiyuan Li, Jason Wang, David Hall, Percy Liang, and Tengyu Ma. Understanding  
 818 warmup-stable-decay learning rates: A river valley loss landscape perspective. October 2024.
- 819 Kaiyue Wen, Zhiyuan Li, Jason Wang, David Hall, Percy Liang, and Tengyu Ma. Understanding  
 820 warmup-stable-decay learning rates: A river valley loss landscape perspective. October 2024.
- 821 Konstantin F Willeke, Paul G Fahey, Mohammad Bashiri, Laura Pede, Max F Burg, Christoph Bless-  
 822 ing, Santiago A Cadena, Zhiwei Ding, Konstantin-Klemens Lurz, Kayla Ponder, et al. The senso-  
 823 rium competition on predicting large-scale mouse primary visual cortex activity. *arXiv preprint*  
 824 *arXiv:2206.08666*, 2022.
- 825 An Yang, Anfeng Li, Baosong Yang, Beichen Zhang, Binyuan Hui, Bo Zheng, Bowen Yu, Chang  
 826 Gao, Chengan Huang, Chenxu Lv, Chujie Zheng, Dayiheng Liu, Fan Zhou, Fei Huang, Feng Hu,  
 827 Hao Ge, Haoran Wei, Huan Lin, Jialong Tang, Jian Yang, Jianhong Tu, Jianwei Zhang, Jianxin  
 828 Yang, Jiaxi Yang, Jing Zhou, Jingren Zhou, Junyang Lin, Kai Dang, Keqin Bao, Kexin Yang,  
 829 Le Yu, Lianghao Deng, Mei Li, Mingfeng Xue, Mingze Li, Pei Zhang, Peng Wang, Qin Zhu, Rui  
 830 Men, Ruize Gao, Shixuan Liu, Shuang Luo, Tianhao Li, Tianyi Tang, Wenbiao Yin, Xingzhang  
 831 Ren, Xinyu Wang, Xinyu Zhang, Xuancheng Ren, Yang Fan, Yang Su, Yichang Zhang, Yinger  
 832 Zhang, Yu Wan, Yuqiong Liu, Zekun Wang, Zeyu Cui, Zhenru Zhang, Zhipeng Zhou, and Zihan  
 833 Qiu. Qwen3 technical report. May 2025.
- 834 Chaoqi Yang, M Westover, and Jimeng Sun. Biot: Biosignal transformer for cross-data learning in  
 835 the wild. *Advances in Neural Information Processing Systems*, 36:78240–78260, 2023.
- 836 Joel Ye and Chethan Pandarinath. Representation learning for neural population activity with neural  
 837 data transformers. *arXiv preprint arXiv:2108.01210*, 2021.
- 838 Joel Ye, Jennifer Collinger, Leila Wehbe, and Robert Gaunt. Neural data transformer 2: multi-context  
 839 pretraining for neural spiking activity. *Advances in Neural Information Processing Systems*, 36:  
 840 80352–80374, 2023.
- 841 Joel Ye, Fabio Rizzoglio, Adam Smoulder, Hongwei Mao, Xuan Ma, Patrick Marino, Raeed Chowd-  
 842 hury, Dalton Moore, Gary Blumenthal, William Hockeimer, et al. A generalist intracortical motor  
 843 decoder. *bioRxiv*, pp. 2025–02, 2025.
- 844 Daoze Zhang, Zhizhang Yuan, Yang Yang, Junru Chen, Jingjing Wang, and Yafeng Li. Brant: Foun-  
 845 dation model for intracranial neural signal. *Advances in Neural Information Processing Systems*,  
 846 36:26304–26321, 2023.
- 847 Yimeng Zhang, T-S Tai Sing Lee, Ming Li, Fang Liu, Shiming Tang, Tai Sing, Lee Ming, Li Fang,  
 848 Liu Shiming, T-S Tai Sing Lee, Ming Li, Fang Liu, and Shiming Tang. Convolutional neural  
 849 network models of V1 responses to complex patterns. *J. Comput. Neurosci.*, pp. 1–22, 2018.
- 850 Yizi Zhang, Yanchen Wang, Donato Jiménez-Benetó, Zixuan Wang, Mehdi Azabou, Blake Richards,  
 851 Renee Tung, Olivier Winter, Eva Dyer, Liam Paninski, et al. Towards a “universal translator” for  
 852 neural dynamics at single-cell, single-spike resolution. *Advances in Neural Information Processing  
 853 Systems*, 37:80495–80521, 2024.
- 854 Yizi Zhang, Yanchen Wang, Mehdi Azabou, Alexandre Andre, Zixuan Wang, Hanrui Lyu, The In-  
 855 ternational Brain Laboratory, Eva Dyer, Liam Paninski, and Cole Hurwitz. Neural encoding and  
 856 decoding at scale, 2025. URL <https://arxiv.org/abs/2504.08201>.
- 857 Yu Zhu, Bo Lei, Chunfeng Song, Wanli Ouyang, Shan Yu, and Tiejun Huang. Multi-modal latent  
 858 variables for cross-individual primary visual cortex modeling and analysis. In *Proceedings of the  
 859 AAAI Conference on Artificial Intelligence*, volume 39, pp. 1228–1236, 2025.

864 A SUPPLEMENTAL RESULTS  
865

866 **OmniMouse enables systematic evaluation of how neuronal context shapes predictive performance.** We evaluated OmniMouse on conditions not seen during training, systematically varying  
867 neuronal history duration (10-25 samples) and population context size (16-2048 neurons) for population  
868 context tasks. Performance scaled smoothly with context availability across all conditions  
869 Fig. S1. When video was available, performance plateaued more quickly for forecasting but continued  
870 to improve for population context, suggesting that nearby neurons carry complementary information  
871 beyond visual input. These systematic evaluations demonstrate that OmniMouse has learned  
872 generalizable representations of neural variability, enabling quantitative assessment of how different  
873 sources of context—temporal history contribute to explaining variability in neural responses.  
874

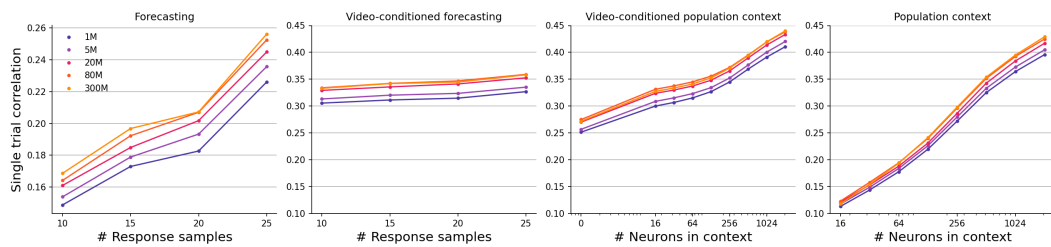
875 Furthermore, we hypothesized that harder tasks might benefit more from scaling, as shown for large  
876 language models (Minaee et al., 2024; Naveed et al., 2025). To test this, we varied the neuronal  
877 history duration (*full-population prefix*  $\in [10, 15, 20, 25]$ ) for forecasting tasks and context size (*context*  
878  $\in [16, 32, \dots, 1024, 2048]$ ) for population context tasks, where shorter contexts represent harder  
879 tasks. We also compared performance with and without 2 seconds of video input. Fig. S1 confirms  
880 our hypothesis: performance improves consistently as context grows, hence, bigger context indicates  
881 easier task. Non-video conditioned regimes scale more steeply, likely due to lower baselines. For  
882 forecasting, they never match video-conditioned models, since video provides temporal information  
883 unavailable at prediction. For population context, however, sufficient neural responses recover  
884 enough information to match video performance. However, contrary to LLMs, in our case scaling  
885 does not preferentially benefit harder tasks: across all tasks, curves for different model sizes remain  
886 parallel. If harder tasks gained more, larger models (20–80M) would show bigger advantages over  
887 smaller ones (1–5M) at minimal context.  
888

889 B RELATION TO OTHER NEUROSCIENCE SCALING.  
890

891 This is the first study to systematically scale both model and data size using only neuro-data, yet  
892 our findings align with prior neuro-scaling work. Consistent with Gokce & Schrimpf (2024), be-  
893 havior prediction improves with larger models, and the greater gains from joint model–data scaling  
894 on non-video tasks (Fig. 7A,B) support claims from Jiang et al. (2025); Ye et al. (2025) that data  
895 heterogeneity limits scaling: our visual stimuli include many repeats, while neural responses vary  
896 with latent brain state and noise even when the visual stimuli is same.  
897

898 C BASELINES  
899

900 To establish baseline comparisons while managing computational costs, we train state-of-the-art  
901 baseline models on the smallest nested dataset containing eight mice (the seven evaluation mice  
902 plus one additional training mouse). This approach ensures that all methods are compared under  
903 identical conditions while keeping baseline training tractable. We train all baselines on 8 recordings  
904



913 **Figure S1: Using the models capabilities to investigate context lengths for forecasting and pop-  
914 ulation context tasks.** **A.** Forecasting with a change of prefix length. **B.** Same change of forecasting  
915 context as **A**, but with video. **C.** Performance improvements in addition to video with population  
916 context. # neurons in context = 0 means the normal "sensorium" task, i.e. video & behavior. Will be  
917 added as an arrow to the panels. Context increases from 0-16-...-2048. **D.** Population context only,  
16 - 2048 neurons

918 from 8 unique mice – 5 fully released mice from the sensorium 2023 competition (keeping the original train-validation-test splits), 2 mice from the sensorium 2022 competition that were used for the test split. session from the MiCRONs collection. The same 8 mice were used in the smallest scaling experiment.  
 919  
 920  
 921  
 922

### 923 C.1 CEBRA 924

925 **CEBRA explanation:** We perform dimensionality reduction on neural activity using InfoNCE  
 926 contrastive learning, where positive and negative pairs are defined by auxiliary variables such as time or  
 927 behavior. When the auxiliary variable is discrete, for example a left or right wheel turn, we select  
 928 positives uniformly from all samples with the same label. When the variable is continuous, such as  
 929 running speed or pupil direction, we choose a random point within a time window around the sample  
 930 and then find the closest match in the dataset using either Euclidean or cosine distance; this sample  
 931 becomes the positive pair, which adds diversity and prevents repeatedly selecting the same example.  
 932 Negative pairs are sampled randomly. For decoding, we encode neural responses, find the nearest  
 933 latent vectors for responses in the training set, and return their associated behavioral variables as  
 934 predictions.

935 **Model hyperparameters:** We trained a joint model for 8 mice, using a batch size of 512 and learning  
 936 rate of  $3 \cdot 10^{-4}$ . The network contained 256 hidden units and produced 128-dimensional outputs  
 937 (both doubled relative to the Allen example [https://cebra.ai/docs/demo\\_notebooks/Demo\\_Allen.html](https://cebra.ai/docs/demo_notebooks/Demo_Allen.html)). Training ran for up to 50,000 iterations with cosine distance as the loss metric. The  
 938 model used a temperature of 1, time-delta conditioning to enable behavior mode, and time offsets of  
 939 5. As CEBRA requires same frequencies between responses and behavior, both were resamples to 20  
 940 Hz, in order to compute correlation on the same predictions as for the OmniMouse. Please note that  
 941 downsampling from 30 Hz responses is not reducing any information as responses were upsampled  
 942 from 6-16 Hz to 30 Hz and the upsampling is done with nearest-neighbor interpolation.  
 943

### 944 C.2 UNIVERSAL SPIKE TRANSLATOR 945

946 **Universal Spike Translator explanation:** The Universal Spike Translator Zhang et al. (2024) per-  
 947 forms a self-supervised modeling approach called multi-task-masking (MtM). The model alternates  
 948 between masking out and reconstructing neural activity across different time steps and neurons. It  
 949 uses a learnable token that provides the model with context about the specific masking scheme that  
 950 is being applied during training, allowing for "mode switching" at test time for different downstream  
 951 tasks. During training, the masking schemes are sampled randomly which are: **(1) Neuron mask-**  
 952 **ing:** Randomly masks individual neurons and reconstructs their activity using the unmasked neurons  
 953 as context. **(2) Causal masking:** Masks future time steps and predicts them using the past steps as  
 954 context.

955 **Model hyperparameters:** We used the default hyperparameters from "ndtl\_stitching\_prompting"  
 956 and "ssl\_session\_trainer" configs from [https://github.com/colehurwitz/IBL\\_MtM\\_model](https://github.com/colehurwitz/IBL_MtM_model).  
 957 Please note that compared to our forecasting settings, IBL does not take behavior as model input.  
 958

### 959 C.3 LATENT DYNAMIC MODEL 960

961 **Latent dynamic model explanation:** This is a probabilistic model that predicts the joint distribu-  
 962 tion of neuronal responses from naturalistic video stimuli and stimulus-independent latent factors.  
 963 Specifically, the model predicts time-varying neuronal response using a Zero-Inflated-Gamma (ZIG)  
 964 distribution to model the distribution of neuronal responses conditioned on the stimulus and the latent  
 965 factor. This is a modification of the deterministic factorized 3D convolutional core and a Gaussian  
 966 readout, where we have an additional encoder that takes a subset of neurons as input to derive a la-  
 967 tent variable. This latent variable is then combined with the transformed visual input to predict the  
 968 activity of other neurons in the session. The model is trained by maximizing the Evidence Lower  
 969 Bound (ELBO) of  $p_{ZIG}(y|x)$  via variational inference.

970 **Model hyperparameters:** For both SENSORIUM 2023 baseline and Schmidt et al. (2025) baseline  
 971 we used the default hyperparameters from Schmidt et al. (2025): 3 layer core with both spatial and  
 972 temporal kernel = 11 in the first layer and 5 on the layer two and three. For more details see App.C  
 973 from Schmidt et al. (2025). All data modalities were upsampled to 30 Hz as both SENSORIUM 2023

baseline and Schmidt et al. (2025) latent model require all modalities to have the same frequencies. Both SENSORIUM 2023 baseline and Schmidt et al. (2025) latent model predict 42 samples from a 60-frame video input, we always used only last 30 frames for evaluation, to make it consistent with OmniMouse, who was trained to predict 30 samples. Please note that OmniMouse support flexible size of predictions, while SENSORIUM 2023 baseline and Schmidt et al. (2025) latent model cannot do it.

#### C.4 IMPLEMENTATION DETAILS

##### C.4.1 MASKING STRATEGIES USED DURING TRAINING

Mask	Behavior	Video (last frames visible)	Visible Neurons	Context (from → to)	Prefix (from → to)	Predicted Behavior
1–3	✓	0	[64, 256, 1024]	0 → 60	—	
4	✗	0	4096	0 → 60	—	✓
5–7	✗	0	[64, 256, 1024]	0 → 60	—	✓
8–19	✓	0	[64, 256, 1024, 4096]	—	[0, 10, 15] → 25	
20–28	✓	0	[64, 256, 1024]	25 → 60	[0, 10, 15] → 25	
29–37	✗	0	[64, 256, 1024]	25 → 60	[0, 10, 15] → 25	✓
38–40	✓	10	[64, 256, 1024]	10 → 60	—	
41–52	✓	10	[64, 256, 1024, 4096]	—	[0, 10, 15] → 25	
53–58	✓	10	[64, 256, 1024, 4096]	25 → 60	[10, 15] → 25	
59–61	✓	20	[64, 256, 1024]	20 → 60	—	
62–73	✓	20	[64, 256, 1024, 4096]	—	[0, 10, 15] → 25	
74–79	✓	20	[64, 256, 1024]	25 → 50	[10, 15] → 25	
80–82	✓	20	[64, 256, 1024]	30 → 60	—	
83–94	✓	30	[64, 256, 1024, 4096]	—	[0, 10, 15] → 25	
95–100	✓	30	[64, 256, 1024]	25 → 40	[10, 15] → 25	
101–103	✓	40	[64, 256, 1024]	30 → 50	—	
104–111	✓	40	[64, 256, 1024, 4096]	—	[10, 15] → 25	
112–114	✓	50	[64, 256, 1024]	30 → 40	—	
115–118	✓	50	[64, 256, 1024, 4096]	—	10 → 20	
119	✓	60	—	—	—	

Table 3: **Summary of training mask configurations.** In each batch all behavior traces for the whole 2 seconds were either given as input or predicted. For each batch 4096 neurons were randomly sampled from  $N$  neurons per mouse and last second (30 responses) for 3072 neurons of these 4096 the activity was predicted.

##### C.4.2 NESTED SCALING DATASET CONSTRUCTION

The nested dataset was constructed such that for the 7 mice we conducted evaluation on - 3 mice we had repeated sessions, such that the number of repeats grew proportionally to the dataset growth, and 4 other mice had a single session. As session-per-mice distribution is highly skewed, the other sessions were samples randomly.

#### C.5 DISTRIBUTION OF SESSIONS PER MOUSE

## D NEUROPHYSIOLOGICAL EXPERIMENTS

Model evaluation was performed on neurophysiological data from Sensorium 2022 ((Willeke et al., 2022), Mouse 1 and 2, evaluation animals for Sensorium and Sensorium Plus tracks) and Sensorium 2023 ((Turishcheva et al., 2024), all animals). Model training was performed on historical data, including data from MICrONS Consortium (2025), Wang et al. (2025), Ding et al. (2025b), Ding et al. (2025a), Fahey et al. (2019), Willeke et al. (2022), Turishcheva et al. (2024), but also included data not previously published.

All procedures were approved by the Institutional Animal Care and Use Committee of Baylor College of Medicine. Seventy-eight mice (*Mus musculus*, 32 females, 46 males, P50–155 on day of

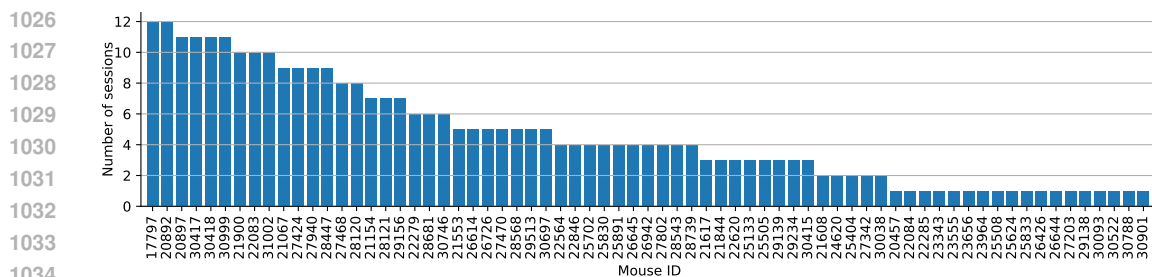


Figure S2: **Distribution of 316 sessions across 69 mice.** More than 100 sessions come from first 10 mice.

first scan) expressing GCaMP6s in excitatory neurons via Slc17a7-Cre and Ai162 transgenic lines (recommended and generously shared by Hongkui Zeng at Allen Institute for Brain Science; Jackson Labs stock 023527 and 031562, respectively) were anesthetized and a 4 mm craniotomy was made over the visual cortex of the right hemisphere as described previously (Reimer et al., 2014; Froudarakis et al., 2014). In two of the seventy-six animals, GCaMP6s was additionally expressed in inhibitory neurons via DLX5-CreER (Jackson Labs stock 010705), following treatment with tamoxifen (orogastric gavage of tamoxifen (Sigma Aldrich T5648) dissolved in corn oil (Sigma Aldrich C8267) at 15 mg/mL, 200 mg/kg body weight, two doses two days apart, second dose  $\geq$  13 days before the first included scan).

Mice were head-mounted above a cylindrical treadmill and calcium imaging was performed using Chameleon Ti-Sapphire laser (Coherent) tuned to 920 nm and a large field of view mesoscope (Sofroniew et al., 2016) equipped with a custom objective (excitation NA 0.6, collection NA 1.0, 21 mm focal length). Laser power after the objective was increased exponentially as a function of depth from the surface according to:

$$P = P_0 \times e^{(z/L_z)} \quad (1)$$

Here  $P$  is the laser power used at target depth  $z$ ,  $P_0$  is the power used at the surface (typically not exceeding 25 mW), and  $L_z$  is the depth constant (160-220  $\mu\text{m}$ ). The greatest laser output of ca. 112 mW was used at approximately 400-500  $\mu\text{m}$  from the surface.

The craniotomy window was leveled with regards to the objective with six degrees of freedom. Pixel-wise responses from an ROI spanning the cortical window (1.7-4 mm diameter FOV, >0.2 px/ $\mu\text{m}$ , superficial cortex, >2.47 Hz) to drifting bar stimuli were used to generate a sign map for delineating visual areas (Garrett et al., 2014). In some but not all cases where the imaging field of view spanned multiple areas, area boundaries on the sign map were manually annotated. Imaging FOV of varying dimensions were targeted to lie within the boundaries of visual cortex, and may span between primary visual cortex and surrounding higher visual areas depending on the scan design.

Scan dimensions typically fell into one of three categories. Local field of view scans contained multiple imaging planes at different depths (10-13 planes, most commonly with 5  $\mu\text{m}$  z spacing but ranging between 3 and 45  $\mu\text{m}$  z spacing), with each plane spanning 600-630  $\times$  600-630  $\mu\text{m}$  (240-252  $\times$  240-252 pixels, 0.4 px/ $\mu\text{m}$  resolution), acquired most commonly at 7.98 Hz (range 4.34-8.31 Hz). Large field of view scans contained single imaging planes at a single depth, with each plane scanning 1.5 - 3 mm diameter (0.33 - 0.4 px/ $\mu\text{m}$  resolution), acquired at between 6.5 - 12.4 Hz. In between are scans containing multiple imaging planes at different depths (2-5 planes, with variable interplane spacing between 5 and 150  $\mu\text{m}$ ), with each plane spanning approximately 0.8-1.2 mm diameter (0.4-0.6 px/ $\mu\text{m}$  resolution), acquired at between 6.3 and 9.6 Hz. Scans with multiple planes, especially at high sampling densities (ex. 5  $\mu\text{m}$  z spacing), have a high likelihood of multiple segmented traces emerging from multiple planes intersecting with the soma of a single neuron in a single scan. Multiple scans were also often collected from the same animal, and as a result single biological neurons may be recorded across multiple scans.

Movie of the animal's eye and face was captured throughout the experiment. A hot mirror (Thorlabs FM02) positioned between the animal's left eye and the stimulus monitor was used to reflect an IR image onto a camera (Genie Nano C1920M, Teledyne Dalsa) without obscuring the visual stimulus.

1080 The position of the mirror and camera were manually calibrated per session and focused on the pupil.  
 1081 Field of view was manually cropped for each session to contain the left eye in its entirety, although  
 1082 across different experiments the field of view may have additionally contained more or less of the  
 1083 face, centered or not centered on the eye, or characterized the pupil at different resolutions. Video  
 1084 was captured at ca. 20 Hz. Frame times were time stamped in the behavioral clock for alignment  
 1085 to the stimulus and scan frame times. Video was compressed using Labview's MJPEG codec with  
 1086 quality constant of 600 and stored in an AVI file.

1087 Light diffusing from the laser during scanning through the pupil was used to capture pupil diameter  
 1088 and eye movements. A DeepLabCut model (Mathis et al., 2018) was trained as previously described  
 1089 (Turishcheva et al., 2024) on 17 manually labeled samples from 11 animals to label each frame of  
 1090 the compressed eye video (intraframe only H.264 compression, CRF:17) with 8 eyelid points and 8  
 1091 pupil points at cardinal and intercardinal positions. Pupil points with likelihood >0.9 were fit with  
 1092 the smallest enclosing circle, and the radius and center of this circle was extracted. Frames with < 3  
 1093 pupil points with likelihood >0.9, or producing a circle fit with outlier > 5.5 standard deviations from  
 1094 the mean in any of the three parameters (center x, center y, radius) were discarded. Gaps in behavior  
 1095 were replaced by linear interpolations over the whole session, if there were more than 2 frames with  
 1096 gaps, then the video is removed.

1097 The mouse was head-restrained during imaging but could walk on a treadmill. Rostro-caudal tread-  
 1098 mill movement was measured using a rotary optical encoder (Accu-Coder 15T-01SF-2000NV1ROC-  
 1099 F03-S1) with a resolution of 8000 pulses per revolution, and was recorded at approx. 50-100 Hz in  
 1100 order to extract locomotion velocity.

1101 Visual stimuli were presented with Psychtoolbox 3 in MATLAB (Brainard & Vision, 1997; Kleiner  
 1102 et al., 2007; Pelli, 1997) to the left eye with a  $31.8 \times 56.5$  cm (height  $\times$  width) monitor (ASUS  
 1103 PB258Q) with a resolution of  $1080 \times 1920$  pixels positioned 15 cm away from the eye. When the  
 1104 monitor is centered on and perpendicular to the surface of the eye at the closest point, this corre-  
 1105 sponds to a visual angle of  $3.8^\circ/\text{cm}$  at the nearest point and  $0.7^\circ/\text{cm}$  at the most remote corner of the  
 1106 monitor. As the craniotomy coverslip placement during surgery and the resulting mouse position-  
 1107 ing relative to the objective is optimized for imaging quality and stability, uncontrolled variance in  
 1108 animal skull position relative to the washer used for head-mounting was compensated with tailored  
 1109 monitor positioning on a six dimensional monitor arm. The pitch of the monitor was kept in the  
 1110 vertical position for all animals, while the roll was visually matched to the roll of the animal's head  
 1111 beneath the headbar by the experimenter. In order to optimize the translational monitor position for  
 1112 centered visual cortex stimulation with respect to the imaging field of view, we used a dot stimulus  
 1113 with a bright background (maximum pixel intensity) and a single dark square dot (minimum pixel  
 1114 intensity). Dot locations were randomly ordered from a grid tiling a portion of the screen, either a  $10$   
 1115  $\times$   $10$  grid tiling a central square (approx.  $90^\circ$  width and height, 10 repeats per location, 200-300 ms  
 1116 presentation at each location), or a  $5 \times 8$  grid tiling the majority of the monitor (approx.  $93^\circ$  height  
 1117 and  $119^\circ$  width, 20 repeats per location, 200 ms presentation at each location). The final monitor  
 1118 position for each animal was chosen in order to center the population receptive field of the scan field  
 1119 ROI on the monitor, with the yaw of the monitor visually matched to be perpendicular to and 15 cm  
 1120 from the nearest surface of the eye at that position.

1120 A photodiode (TAOS TSL253) was sealed to the top left corner of the monitor, and the voltage was  
 1121 recorded at 10 kHz and timestamped on the behavior clock (MasterClock PCIe-OSC-HSO-2 card).  
 1122 Simultaneous measurement with a luminance meter (LS-100 Konica Minolta) perpendicular to and  
 1123 targeting the center of the monitor was used to generate a lookup table for linear interpolation between  
 1124 photodiode voltage and monitor luminance in  $\text{cd}/\text{m}^2$  for 16 equidistant values from 0-255, and one  
 1125 baseline value with the monitor unpowered.

1126 At the beginning of each experimental session, we collected photodiode voltage for 52 full-screen  
 1127 pixel values from 0 to 255 for one second trials. The mean photodiode voltage for each trial  $V_{pd}$  was  
 1128 fit as a function of the pixel intensity  $V_{in}$ :

$$V_{pd} = B + A \times V_{in}^\gamma \quad (2)$$

1129  
 1130 in order to estimate the  $\gamma$  value of the monitor ( $\approx 1.50 - 1.76$ ). All stimuli were shown with no  $\gamma$   
 1131 correction.

1134 During the stimulus presentation, sequence information was encoded in a 3 level signal according to  
1135 the binary encoding of the flip number assigned in-order. This signal underwent a sine convolution,  
1136 allowing for local peak detection to recover the binary signal. A linear fit was applied to the trial  
1137 timestamps in the behavioral and stimulus clocks, and the offset of that fit was applied to the data to  
1138 align the two clocks, allowing linear interpolation between them. The mean photodiode voltage of  
1139 the sequence encoding signal at pixel values 0 and 255 was used to estimate the luminance range of  
1140 the monitor during the stimulus, with typical maximum values of approx. 10-12 cd/m<sup>2</sup>.

1141

1142

1143

1144

1145

1146

1147

1148

1149

1150

1151

1152

1153

1154

1155

1156

1157

1158

1159

1160

1161

1162

1163

1164

1165

1166

1167

1168

1169

1170

1171

1172

1173

1174

1175

1176

1177

1178

1179

1180

1181

1182

1183

1184

1185

1186

1187